The Brookhaven muon storage ring magnet[☆]

G.T. Danby[a], L. Addessi[a], Z. Armoza[a], J. Benante[a], H.N. Brown[a], G. Bunce[a,*],
J.C. Cottingham[a], J. Cullen[a], J. Geller[a], H. Hseuh[a], J.W. Jackson[a], L. Jia[a], S. Kochis[a],
D. Koniczny[a], R. Larsen[a], Y.Y. Lee[a], M. Mapes[a], R.E. Meier[a], W. Meng[a],
W.M. Morse[a], M. O'Toole[a], C. Pai[a], I. Polk[a], R. Prigl[a], Y.K. Semertzidis[a], R. Shutt[a],
L. Snydstrup[a], A. Soukas[a], T. Tallerico[a], F. Toldo[a], D. Von Lintig[a], K. Woodle[a],
R.M. Carey[b], W. Earle[b], E.S. Hazen[b], F. Krienen[b], J.P. Miller[b], J. Ouyang[b],
B.L. Roberts[b], L.R. Sulak[b], W.A. Worstell[b], Y. Orlov[c], D. Winn[d], A. Grossmann[e],
K. Jungmann[e], G. zu Putlitz[e], P. von Walter[e], P.T. Debevec[f], W.J. Deninger[f],
D.W. Hertzog[f], S. Sedykh[f], D. Urner[f], M.A. Green[g], U. Haeberlen[h], P. Cushman[i],
S. Giron[i], J. Kindem[i], D. Miller[i], C. Timmermans[i], D. Zimmerman[i],
V.P. Druzhinin[j], G.V. Fedotovich[j], D.N. Grigorev[j], B.I. Khazin[j], N.M. Ryskulov[j],
S. Serednyakov[j], Yu.M. Shatunov[j], E. Solodov[j], K. Endo[k], H. Hirabayashi[k],
Y. Mizumachi[k], A. Yamamoto[k], S.K. Dhawan[l], A. Disco[l], F.J.M. Farley[l], X. Fei[l],
M. Grosse-Perdekamp[l], V.W. Hughes[l], D. Kawall[l], S.I. Redin[l]

[a]Brookhaven National Laboratory, Upton, NY 11973, USA
[b]Department of Physics, Boston University, Boston, MA 02215, USA
[c]Newman Laboratory, Cornell University, Ithaca, NY 14853, USA
[d]Fairfield University, Fairfield, CT 06430, USA
[e]Physikalisches Institut der Universität Heidelberg, 69120 Heidelberg, Germany
[f]Physics Department, University of Illinois at Urbana-Champaign, Urbana-Champaign, IL 61801, USA
[g]Lawrence Berkeley Laboratory, Berkeley, CA 94720, USA
[h]Max Planck Institiut für Medizinische Forschung, 69120 Heidelberg, Germany
[i]Department of Physics, University of Minnesota, Minneapolis, MN 55455, USA
[j]Budker Institute of Nuclear Physics, Novosibirsk, Russia
[k]KEK, High Energy Accelerator Research Organization, Tsukuba, Ibaraki 305-0801, Japan
[l]Department of Physics, Yale University, New Haven, CT 06511, USA

Abstract

The muon g-2 experiment at Brookhaven National Laboratory has the goal of determining the muon anomalous g-value a_μ ($= (g - 2)/2$) to the very high precision of 0.35 parts per million and thus requires a storage ring magnet with great stability and homogeniety. A superferric storage ring with a radius of 7.11 m and a magnetic field of 1.45 T has been constructed in which the field quality is largely determined by the iron, and the excitation is provided by superconducting coils operating at a current of 5200 A. The storage ring has been constructed with maximum attention to azimuthal symmetry and to tight mechanical tolerances and with many features to allow obtaining a homogenous magnetic field. The fabrication of the storage ring, its cryogenics and quench protection systems, and its initial testing and operation are described. © 2001 Elsevier Science B.V. All rights reserved.

1. Introduction

This article describes the storage ring magnet built for the muon g-2 experiment at the Brookhaven National Laboratory AGS, shown in Fig. 1. The goal of the experiment is to measure the anomalous magnetic moment of the muon to 0.35 parts per million of itself (ppm). The experiment is done similar to the beautiful CERN experiments [1],[1] with a goal of a factor of 20 greater precision. The technique involves storing 3.094 GeV/c muons in a uniform magnetic field. The energy is selected to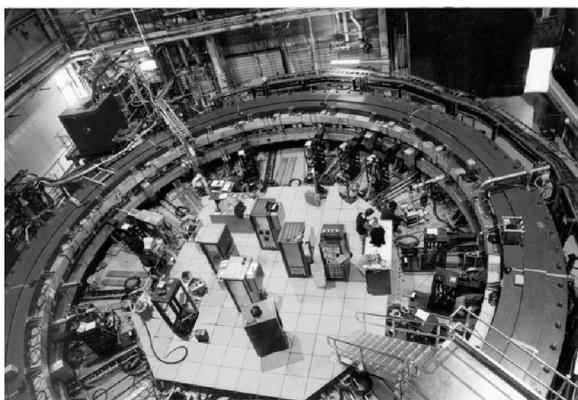 be at the "magic gamma", where electric fields can be used to focus and contain the muons in the storage ring without disturbing the measurement of the muon anomaly to first order. The CERN experiment used 40 dipole magnets to form a storage ring 14 m in diameter, and the magnetic field was known to 1.5 ppm. The BNL storage ring has been built as a single continuous magnet, also 14 m in diameter, with the magnetic field to be known to 0.1 ppm. The magnet was designed to produce a field as uniform as possible, both azimuthally and over the storage ring aperture. A very uniform field reduces requirements on the knowledge of the locations of the magnetic field probes, and on the stored muon distribution. Shimming the magnetic field to the required uniformity will be discussed in a future paper; here we present the design, construction details, and operating parameters of the muon storage ring magnet.

Fig. 1. Photograph of the muon g-2 storage ring magnet at Brookhaven.

2. Magnet design

A 1.451 T magnetic field constrains the 3.094 GeV/c muons to move in a circle with a central orbit radius of 7.112 m. The storage region itself has a cross-sectional diameter of 9 cm. The average magnetic field as seen by the stored muons must be known to 0.1 ppm. Since the distribution of the stored muons cannot be measured to great precision, the goal of the experiment was to produce a magnet of about 1 ppm uniformity over the muon storage aperture, averaged over azimuth. (The

---

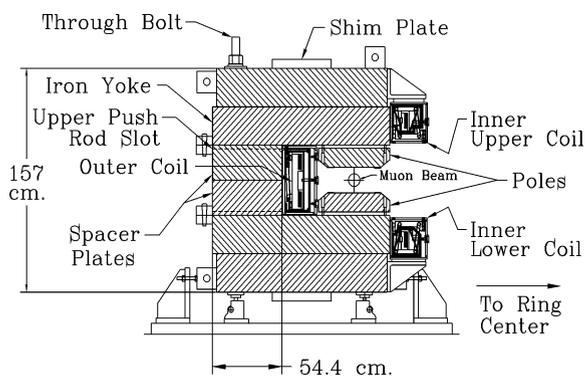[1] Their final result: was $a_\mu = 11659230(84) \times 10^{-10}$.

Fig. 2. A cross-section view of the magnet.

muons average over azimuth.) The additional factor of 10 improvement in knowledge of the field can be gained by folding the muon distribution with an accurate measurement of the field in the storage ring volume. Uniformity in azimuth is also desirable to improve the NMR measurements and simplify the analysis of the average field seen by the muons. The CERN experiment had a 200 ppm variation in azimuth, 15 ppm (rms) uniformity over the cross-section, and achieved a 0.5 ppm error in the field for the g-2 measurement [2]. Hence, very stringent requirements on B-field homogeneity and stability dominate the design of the ring.

The storage ring is built as one continuous super-ferric magnet, an iron magnet excited by superconducting coils. A cross-section of the magnet is shown in Fig. 2. The magnet is C-shaped as dictated by the experiment requirement that decay electrons be observed inside the ring. The field, and hence its homogeneity and stability, are determined dominantly by the geometry, characteristics, and construction tolerances of the iron. Although both copper and superconducting coils were considered, the use of superconducting coils offered the following advantages: thermal stability once cold; relatively low power requirements; low voltage, and hence use of a low-voltage power supply; high L/R time constant value and hence low ripple currents; and thermal independence of the coils and the iron. The main disadvantage was that the coils would have a much larger diameter and smaller height than any previously built superconducting magnet. However, since we could not identify any funda-

mental problems other than sheer size, we decided to build superconducting coils.

To obtain the required precision in such a large diameter magnet with an economical design is an enormous challenge. The magnet had to be a mechanical assembly from subpieces because of its size. With practical tolerances on these pieces, variations up to several thousand ppm in the magnetic field could be expected from the assembled magnet. To improve this result by two to three orders of magnitude required a design which was a "shimable kit" [3].

Because of the dominant cost of the yoke iron, it was an economic necessity to minimize the total flux and the yoke cross-section. This led to a narrow pole, which in turn conflicts with producing an ultra-uniform field over the 9 cm good field aperture.

A simple tapered pole shape was chosen which minimized variations in the iron permeability and field throughout the pole. The ratio of pole tip width to gap aperture is only $\frac{2}{1}$. This results in a large dependence of the field shape with the field value B [3]. However, since the storage ring is to be used at only one field, $B = 1.45$ T, this is acceptable. Because of dimensional and material property tolerance variation, the compact pole increases the necessity for a simple method of shimming.

Experience with computer codes, in particular with POISSON [4], had demonstrated that, with careful use, agreement with experiment could be expected at a level of 10^{-4} accuracy. POISSON is a two-dimensional (2D) or cylindrically symmetric code, appropriate for the essentially continuous ring magnet chosen for the g-2 experiment. Computational limitations, finite boundary conditions, and material property variations are all possible limitations on the accuracy of "paper" designs.

A considerable effort was put into refining the computer calculations as the design progressed to obtain reproducable convergence to very high accuracy. The field in the aperture is expressed in terms of multipoles in Table 1 for the 2D version of POISSON. The description of the field using multipoles reproduced the computed field to considerably better than 1 ppm, indicating internal consistency in the fit. Expressing the field in multipolar symmetries is a great aid to design

Table 1

Multipoles for the 2D magnet baseline design at $r = 4.5$ cm, the storage ring boundary. The baseline design uses ultra-low-carbon steel plate (ULCS) for the poles (permeability 1450 at 1.6 T field) and AISI 1006 steel for the yoke (permeability 540 at 1.6 T). In addition to the multipoles in the first column, δ is the difference between the multipole reconstructed field, to $n = 8$, from the computed field, at $r = 4.5$ cm on the horizontal midplane (HMP) and vertical midplane (VMP). Column 2 shows the baseline design computation. For the baseline design, the multipoles were so small that further optimization was not useful, since as-built variations were expected to be (and were) larger and needed to be shimmed out. The other columns show differences for changes indicated. Column 3 shows the field change using ULCS for the yoke in place of AISI 1006; column 4 shows the effect of a change in each shimming air gap of -0.1 mm (which changes the total air gap by $-1/1000$); and column 5 shows the effect from a translation of the poles toward the yoke by 0.1 mm, keeping the total air gap constant

	Baseline	UCLS yoke	$\Delta_{\text{shim gap}} = -0.1$ mm	$\Delta_{\text{pole ht}} = -0.1$ mm
Dipole (r^0)	1.45 T	$\Delta B = 1250$ ppm	$+690$ ppm	-35 ppm
Quadrupole (r^1)	-16.3 ppm	-24.5 ppm	-0.05 ppm	$+0.6$ ppm
Sextupole (r^2)	-2.1 ppm	-34.6 ppm	-0.3 ppm	-1.1 ppm
Octupole (r^3)	0 ppm	-1.5 ppm	-0.02 ppm	-0.05 ppm
r^4	0 ppm	-1.1 ppm	-0.02 ppm	-0.2 ppm
r^5	0 ppm	-0.1 ppm		-0.03 ppm
r^6	-1.0 ppm	1.1 ppm		-0.01 ppm
r^7	≈ 0 ppm	≈ 0 ppm		
r^8	≈ 0 ppm	≈ 0 ppm		
$\delta(4.5\text{ cm})_{\text{HMP}}$	$+0.14$ ppm			
$\delta(4.5\text{ cm})_{\text{VMP}}$	0.00 ppm			

optimization of the field in the 9 cm aperture. The ratio of aperture to ring diameter is so small that there is only a very small difference between the 2D computed field shape and the three-dimensional (3D) field shape. 3D field computations verified this. The difference is much smaller than the practical errors that occur in the actual magnet, which must be shimmed out in any case.

The removable edge shims on the pole surfaces play a major role in the design of the magnet and its eventual actual shimming corrections. As seen in Fig. 3, the edge shims are symmetrically located about the aperture center line. Various symmetric perturbations of the shims produce predictable multipoles. For example, changing equally all four corners produces only sextupole series terms, proportional to even powers of the aperture radius. Increasing the two outside shims and/or decreasing the inside shims produce only normal quadrupole series terms, proportional to odd powers of the aperture radius. This can be extended to up-down and diagonal (skew) asymmetries. These mathematically predictable asymmetries were indeed found to apply to very high accuracy, including linear
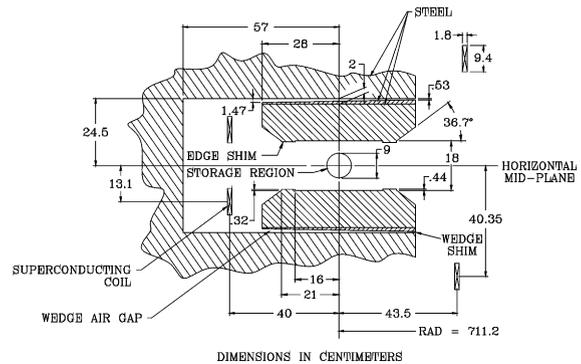
Fig. 3. A cross-section view of the magnet gap region.

superpositions for finite permeability, again showing internal consistency in the computations.

Finite and realistic permeability was then used, and the amplitudes of the corner shim perturbations were progressively raised. It was found that the multipole description was still correct and increased linearly with amplitude until unrealistically strong edge shims finally gave a breakdown in linearity as well as in the required symmetries. This

gave confidence that the computer calculations could be used to get the design optimization on paper, and also to calculate multipole perturbations of the operating magnet, to correct the field to approaching a 1 ppm level.

Wedge-shaped air gaps between the poles and yoke are an important design feature. These air gaps sufficiently isolate the precision poles from the yoke return that field aberations, or multipoles above the dipole term, are minimally affected by reasonable variations in the yoke reluctance (Table 1). Since the poles dominate the field aberations, the highest quality of iron is only required for the poles. Very pure continuous cast steel is used for the poles. This material is typically of 0.004% carbon content. The higher purity increases permeability at the operating field of the magnet compared to conventional AISI 1006 iron (0.07% carbon typically), which is used for the yoke. Even more important is the impact of the purity on inclusions of ferritic or other extraneous material, air bubbles, etc., which are greatly minimized.

This isolation of field aberations from dipole reluctance has an additional very important property. It is necessary to have large holes through the yoke to inject the beam, for inflector power and cryogens, and for the outer coil leads and cooling. Because of the isolation from the air gaps, no significant effect on multipoles is observed after restoring the reluctance in the region of the holes by adding large iron collars [5].

The air gaps are wedge-shaped, with a larger air gap on the outer radius, closest to the iron return of the C magnet. The slope is calculated to compensate for the gradient due to C magnet asymmetry (Fig. 2), where the field lines would otherwise tend to cross the gap near the return. Calculations showed that a change in wedge angle caused a very pure normal quadrupole adjustment without inducing higher multipoles. A change in the wedge slope by 1 mm over the length of the wedge changes the quadrupole (at 4.5 cm, the edge of the storage volume) by 15 ppm, while the sextupole term changes by 1 ppm, and the higher multipole changes are still smaller. Attempting to make a large quadrupole adjustment by using pole edge shims introduces octupole, roughly half the size of the quadrupole change [5]. Instead, a combination of

wedge angle and inside–outside asymmetry in edge shims can null both quadrupole and octupole.

The inner radius coils, required to be away from the midplane to allow observation of decay electrons from the stored muons, were pulled still further vertically away from the midplane in order to have access to the air gaps for shimming. This has the additional advantage of making the hoop force on these large diameter slender inner coils approximately zero.

The final coil design used a single layer of the KEK TOPAZ pure aluminum stabilized superconductor [6] to excite the 20 cm air gap. The iron circuit dominates so strongly that tolerances on coil location are quite reasonable, as discussed below.

Final pole design involved refinements to the edge shims plus adjustments of the location and angle of the taper of the edges of the poles. To first order, to flatten the field, the cross-sectional area of the edge shims is the important parameter. However, in detail the distance of the inner edge of the shims to the center (Fig. 3), chosen to be $r = 16$ cm, and the shim width of $r = 5$ cm, optimized the field quality by reducing the r^6 multipole. This in combination with an edge angle of $36.7°$ produced a very small r^2 sextupole, the r^4 term was nulled, and all higher multipole terms were virtually eliminated.

Making the wedge separate from the poles presented some mechanical complications, but resulted in substantial shimming advantages. A change in the air gap, changing the wedge thickness with no change in angle, produces a very strong effect on the local dipole field, essentially proportional to the thickness change divided by the half-gap of 10 cm. This is because the storage ring aperture and air gaps at the base of each pole constitute 93% of the circuit reluctance. However, small vertical movements of the poles have a small effect on the reluctance, since the combined air gap is unchanged (Table 1).

Errors in the precision pole thickness are small compared to the expected variation of up to 200 μm in the distance between the top and bottom yoke plate surfaces adjacent to the poles.

A means of shimming in the air gaps is attractive, since only dipole is affected, and not higher
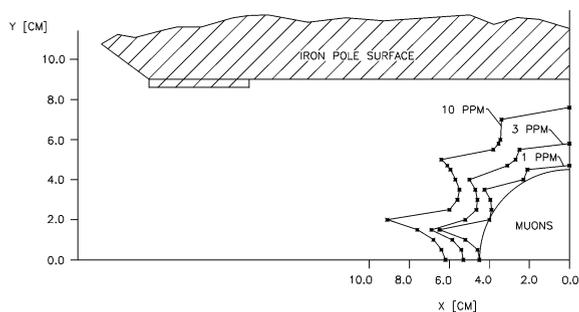
Fig. 4. Computed field variations for the magnet design.

multipoles. The average thickness of the wedges determines dipole, and the wedge angle determines quadrupole, both essentially pure moments. Finally, if the wedges are radially adjustable, a very fine control for dipole exists. Since the wedge angles are approximately $\frac{1}{50}$, radial movement by 50 μm changes the gap by 1 μm, finer control than is available otherwise.

At least on paper, and using realistic parameters, a magnet aperture of 9 cm diameter was designed with a uniform field to a ppm level (Fig. 4).

Long-wavelength "real world" errors will be greatest for low-order moments, both normal (field vertical on the horizontal midplane) and skew. The shimming techniques described are designed to correct most of these, with surface coils required to correct skew dipole.

Correcting coils on the surface of the poles permit ultimate fine control of static, and slowly varying errors. The surface coils can be used to correct lowest multipoles to tens of ppm, thus providing significant overlap between the iron shimming and the dynamic shimming. These coils have been constructed to generate moments over the entire 360° azimuth. The coils were designed with printed circuit boards, with 2×120 wires running azimuthally around the ring on the top and bottom pole surfaces facing the storage ring gap, and spaced radially 2.5 mm apart, to avoid lumpy effects which generate higher multipoles. Pole surface corrections can be (and have been) added with ferromagnetic material to correct for local effects in the iron geometry. Local current loops may also be used. The "continuous" ring was built with 10° pole sections, 36 of which form an almost continuous ring. Dipole

correction coils are located in the air gaps for each 10° pole.

Strictly speaking, the description of the storage ring field aberations by multipoles assumes no gradients in the beam direction. However, the muon betatron wavelengths are very long so that longitudinal averaging of actual field data is correct to a very good approximation. For example, for a 10° pole section the azimuthal integral of field data can give an average multipole fit to very good accuracy. The pole edge shims or other adjustments can be applied to correct this 10° average.

Computations of a 75 μm crack between the 10° poles show that the dipole field is reduced slightly locally, but the longitudinal integral was independent of both r and y, so the effect was only on the field integral and not on the field aberations.

There are limits to averaging out local field irregularities in the poles, one of which is simply that the ability to measure precisely is more difficult with large gradients. Thus, the g-2 storage ring shimming effort has the goal to make the field as uniform as practical.

Fig. 5 shows the magnetic field lines for the design, and the magnet parameters are given in Table 2.

3. Magnet construction

3.1. Construction of the superconducting coils

The magnet is powered by three superconducting coils, as shown in Fig. 2. The coil at the outer radius drives the field across the storage ring gap, and the
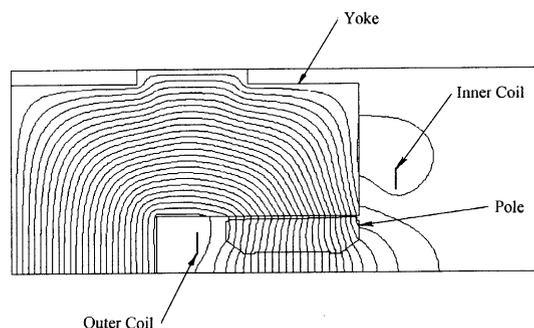

Fig. 5. Computed magnetic flux lines for the magnet.

Table 2
Magnet parameters

Design magnetic field	1.451 T
Design current	5200 A
Equilibrium orbit radius	7112 mm
Muon storage region diameter	90 mm
Inner coil radius – cold	6677 mm
Inner coil radius – warm	6705 mm
Outer coil radius – cold	7512 mm
Outer coil radius – warm	7543 mm
Number of turns	48
Cold mass	6.2 metric tons
Magnet self inductance	0.48 H
Stored energy	6.1 MJ
Helium-cooled lead resistance	6 $\mu\Omega$
Warm lead resistance	0.1 mΩ
Yoke height	157 cm
Yoke width	139 cm
Pole width	56 cm
Iron mass	682 metric tons
Nominal gap between poles	18 cm

two coils at the inner radius, above and below the midplane, cancel the flux in the ring center and improve the field quality in the gap. The outer coil carries 5200 A with 48 turns. It is split into two blocks, above and below the midplane, to allow the beam to enter the storage ring. The inner coils are each 24 turns, connected in series with the outer coil, with the reverse current direction.

The mechanical design of any superconducting magnet must provide support for the coils against the large Lorentz forces, and at the same time result in little heat load. The superconducting coils needed to be held in a way that would avoid stick–slip conditions when powering the magnet which could lead to quenching the magnet. The coil locations needed to repeat to ± 0.5 mm in radius, to maintain the required field quality. The field is relatively insensitive to the coil position. A local radial shift of 1 mm changes the dipole field by 116 ppm, but the muon trajectories in the storage ring average over the azimuth, so that the change in average dipole field due to radial shifts of the coil tends to cancel. Quadrupole, sextupole and octupole terms are changed by less than 0.1 ppm for a 1 mm radial shift. For a vertical shift in outer coil mandrel position, one coil block shifts away from the midplane, and one coil block shifts toward the

midplane, which cancels the effect on the field to first order, leaving less than 1 ppm dipole change, and less than 0.1 ppm change for higher multipoles for a 1 mm shift. The effect of shifts of the inner coils is smaller yet [5].

The large coil diameter and small height presented both design and construction concerns. The coils easily deform elastically in the radial direction, and also vertically. Furthermore, the coils shrink 30 mm in radius during cooldown, and the outer coil then expands in radius 3 mm when powered. These made the design of a coil support and locating system difficult.

The coil design was based on the TOPAZ solenoid at KEK [6]. TOPAZ conductor was used, with pure aluminum stabilizer and niobium–titanium superconductor in a copper matrix. Conductor characteristics are given in Table 3. At full field the critical temperature of the outer coil is 6.0 K. The magnet typically operates at 5.0 K. This represents 76% of the superconductor limit. Each coil block is effectively a very short solenoid with 24 turns, and one layer. The coils are wound from the inside of the ring so that, when powered, the coils push out radially against a massive aluminum mandrel. Cooling is indirect with helium pipes attached to the mandrels. The coil turns, coil stack and insulation are epoxied together, forming a monolithic block. The coils hang from the cryostat with low heat load straps, and the shrinkage and expansion of the coils is taken by the straps. The coils are located using radial stops on the inner radius. For the outer coil the stops transfer the force from the

Table 3
Conductor parameters

Superconductor type	NbTi/Cu
Nominal dimensions	1.8 mm × 3.3 mm
NbTi/Cu ratio	1:1
Filament	50 μm
Number of filaments	1400
Twist pitch	27 mm
Aluminum stabilizer type	Al extrusion
Ni/Ti composite dimensions	3.6 mm × 18 mm
Al/(NbTi + Cu) ratio	10
RRR (Al)	2000–2500
RRR (Cu)	120–140
I_c	8100 A (2.7 T, 4.2 K)

coil to the cryostat box, and push rods from the iron yoke transfer the force from the box to the iron. For the inner coils, pins replace the pushrods.

3.1.1. Mandrel construction and coil winding

The coils were built in the g-2 experimental building with a floor area only somewhat larger than the ring. The coils were constructed in sequence: each of the three coils was wound and transported outside for temporary storage, followed by construction of each cryostat/coil assembly. These assemblies were stored outside during construction of the bottom half of the iron yoke. The transfers were done using a fixture which supported the coil circumference, and interior and exterior cranes. The fixture included wheels which rolled on tracks to pass the coil through a slot built into the side of the building (Fig. 6).

Fig. 7. The coil winding fixture, shown on the turntable. An inner coil is being wound.

Coil construction was based on a large turntable with a 2.4 m radius, rated for a 36 metric ton non-eccentric loading (Fig. 7). It was powered by a 15 hp motor with a drive ranging from 0.005 to 0.3 revolutions per minute. An additional platform extended the working radius to 6.7 m for the inner coils and 7.5 m for the outer radius coils. A track supported the outer end of the platform, with a 0.5 mm vertical runout maximum. The turntable supported a milling machine and the coil winder. The construction of the outer coil is described here, with significant differences in inner coil construction noted.

The aluminum mandrel (Fig. 8) supports compressive conductor preload, it supports the coil

Fig. 6. The completed outer coil and cryostat were passed through the slot in the g-2 building and stored outside, in preparation for construction of the lower half of the magnet yoke. The completed inner coils in their cryostats are in the foreground.
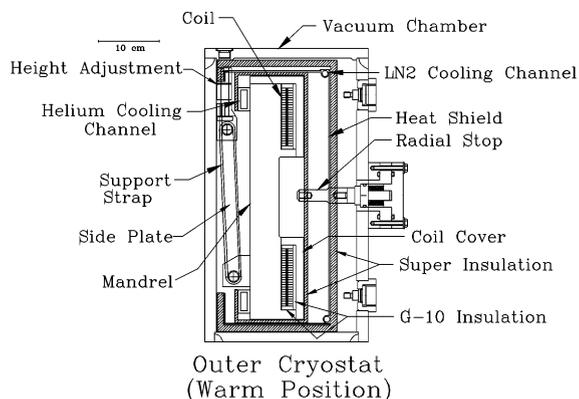

Fig. 8. A cross-section of the outer coil and cryostat assembly at the location of a radial stop.

against the Lorentz force, and it indirectly cools the superconductor via liquid helium carried in tubes welded to the mandrel outer radius. The mandrel cross-section includes an inner radius ledge for each coil block. The outer mandrel cross-section was chosen to limit expansion under Lorentz force to 3 mm radius. The mandrel was built from 12 sections, which were rolled to shape, finish machined on outer radius and bottom, and rough machined on inner radius and top. The bending process proved difficult, due to the asymmetry from the ledges. Machining, bending, heat treating to remove stresses, and rebending were necessary. An independent ledge piece, attached to the mandrel, may have been a better approach. The 12 sections were then joined with full penetration welds of the 50 mm thick outer mandrel, using a massive weld fixture and a combination of MIG and TIG welds. Peening of the weld joint between each welding pass while hot was essential to minimize distortion. The milling machine on the turntable was used to complete the inner winding surface and mandrel top.

In the next step, the rectangular tubes for the liquid helium were stitch-welded to the mandrel, using alternate welds 2.5 cm long, above and below the tube and leak tested. Leak testing was particularly important because the coils are inaccessible. The tubes were cycled to liquid nitrogen temperature twice, warming to room temperature in between. A vacuum leak check was performed where the tube was evacuated and helium was sprayed onto every joint from the outside. The last step was to pressurize the tube to 250 psi with helium gas, and to check each joint by bagging each region for 10 min, then sniffing the bag.

At this point, the mandrel was prepared for winding. A ground plane insulation band of 0.3 mm thickness was built from a sandwich of three layers of 50 μm kapton, epoxy coated, between two layers of epoxy-filled fiberglass. The insulation assembly was fully cured and placed into the mandrel. A 0.1 mm layer of B-stage epoxy film was placed between the mandrel and kapton laminate, and between the kapton laminate and the conductor block after winding. A 4.8 mm thick G-10 piece was placed on the winding ledge, and on top and on the inner radius of the completed coil block. The insulation protected against a local failure in an insulation layer and against creep failure along a surface. The epoxy-filled fiberglass in the ground plane insulation sandwich improved heat transfer between coil and mandrel.

The coil winder was then installed on the turntable, as shown in Fig. 7. This device included a single conductor width spool with 1 km of conductor, a caterpillar drive which applied 625 N of compressive force to the conductor, a 3-head insulation-wrapping machine, the insulation test stand, and guides which bent the wide dimension of the conductor to a 1.5 m radius, approaching the mandrel at a $10°$ downward angle. A last guide reshaped the conductor to the nominal radius and supported the conductor into the mandrel. The conductor feed device automatically adjusted the height for each of the 24 layers. A 1.4 m long G-10 ramp at the end of the first layer provided a spiral wind to the second layer. Long sections of conductor were left at both ends of the wind to form the leads to connect in series with the other coils and to the cold to warm transition or lead pot.

Turn-to-turn insulation used three overlapping layers of kapton (25 μm each) and fiberglass filled with B-stage epoxy, 19 mm in width. Layers were helically wrapped around the conductor with 0–0.8 mm between turns; each of the three layers were offset by 6.4 mm. This wrap was applied and tested at 2000 V DC during the wind.

The winder typically ran at 0.6 m/min. During the operation, closely spaced pneumatic vertical clamps automatically extended to press on the top surface of the conductor to preclude buckling as the conductor was pushed against the mandrel. The method of winding, applying the conductor to the inside of a mandrel, results in the mandrel absorbing the outward Lorentz force of the coil.

After the 24th layer, the conductor was shaped away from the coil block to be used as a lead. Aluminum covers were then added in 90 cm sections, including top and inner radius insulation as mentioned. The covers restrain the coil radially and vertically, and act as a heat shield to isolate the coils. Electrical strip heaters, attached temporarily to the mandrel and covers along with an outer wrap of fiberglass insulation, were used to cure the epoxy. Spring-loaded clamps compressed the covers during the cure. A temperature of $125°C$ was

used for 1 h. For the outer coil, each block was wound and cured separately, so that the lower coil block received two heating cycles. This procedure had been found in tests to be acceptable for the epoxy and the temperature is well below 400°C where superconductor deteriorates. Extensive tests developed the correct amount of epoxy needed to completely fill the coil blocks without voids.

The spring clamps assured that the covers were forced to their final position for bolting, so as to apply both a vertical prestress to enhance heat conduction between conductor layers, and a radially outward prestress of the coil block into the mandrel. This radial preload of $1.8–2.2 \times 10^4$ N/m circumference was used to assure no local coil motion during powering, where the Lorentz force is 7×10^4 N/m outward for the two outer coil blocks together and 1×10^3 N/m inward for the inner coils at full field.

3.1.2. Cryostat assembly

The coil cryostats provide the insulating vacuum, coil suspension and positioning, heat shields and superinsulation, and cooling and electrical connections. The cryostat box must allow for the 30 mm radial shrinkage of the coil from cooldown, with repeatable coil positioning.

An insulating vacuum of 10^{-5} Torr was required. All welded construction was used. The boxes were constructed using 6061 T-6 aluminum alloy plate. Inner coil cryostat walls are 1.2 cm thick; outer coil cryostat side walls are 1.9 cm thick, and top and bottom walls are 1.6 cm thick. U-sections were formed in azimuthal sectors (16 sectors outer, 12 sectors inner) and welded to form an open box in a continuous circle.

At this stage, the coil was brought back into the building and suspended above the open cryostat. Fig. 8 shows the components in an outer coil cryostat assembly. Hangers were attached to the coil. Blankets of superinsulation were wrapped around the coil, the heat shield built in place, and additional superinsultation added. The coil was then lowered into the cryostat, the straps attached to the cryostat, and the cryostat covers were welded on.

The hanging straps [7] are racetrack shaped, 2 cm wide, 26 cm long, and 2.5 cm across. They were built at Brookhaven from multifilament fiberglass and B-stage epoxy. The straps have high tensile strength (1×10^9 Pa) and low thermal conductivity. The heat leak for one strap is calculated to be 0.14 W. For the outer coil and upper inner coil, side plates were added for compressive strength: the outer coil vertical force is unstable about the midplane, and the upper inner coil vertical force is upward, opposite gravity. The suspension arrangements were different for the outer and inner coils. For the outer coil, one strap was used to hang the coil from the outer radius of the cryostat box, at 16 azimuthal locations. This is shown in Fig. 8. At room temperature, the outer coil hangs with the straps vertical. When cooled, the coil shrinks 30 mm in radius and the coil rises 3.3 mm. When powered, the outer coil expands 3 mm in radius, and the nominal hanger angle is 10° inward from vertical. The vertical Lorentz force is unstable, 5×10^2 N/m in circumference per mm vertical displacement away from the midplane. The outer coil center was originally placed to be 0.5 mm below the midplane powered. The final offset, done after we found that some of the coil rose above the midplane during initial magnet testing, was 1.5 mm below the midplane powered.

The inner coils hang from pairs of straps at 48 azimuthal locations. The strap angles, when powered, are vertical, Fig. 9. For this geometry, a radial misalignment, either inward or outward, leads to a vertical displacement and a strong vertical restoring force. The vertical Lorentz force gradient for the inner coils is 2×10^3 N/m in circumference per mm vertical displacement away from the midplane. The radial force gradient is 1×10^2 N/m per mm outward for an outward displacement.
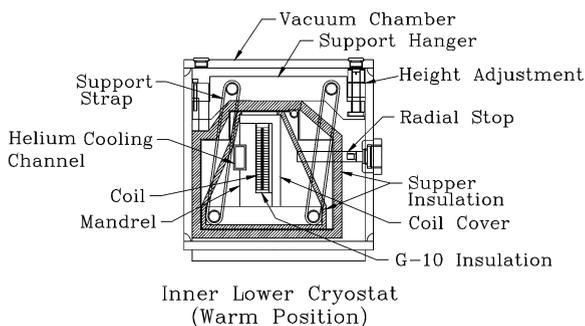

Fig. 9. An inner coil assembly cross-section.

We discussed a number of ways to set a repeatable coil position, using either passive or active (such as driven by solenoids) radial locators, the difficulty being the large radial shrinkage during cooldown, and expansion during powering. We chose a passive coil positioning system of stops, attached to the inner radius walls of the cryostats. The stops are set to just touch the coils when powered. When cooled, before powering, the coil takes on a scallop shape, since the stops are at a larger radius than the average coil radius. For the outer coil, this difference is 3 mm; for the inner coils it is 0.1 mm. The force on the outer coil cryostat inner wall is transmitted to the iron yoke by preloading the cryostat from the outer radius with pushrods. Pushrods at the top and bottom of the cryostat extend from the outer radius of the yoke in slots, and compress the cryostat radially. Strain gauges on the pushrods show that the preload becomes less as the outer coil cools down, pressing against the radial stops. For the inner coils, the force when cold and unpowered is small, and fixed pins are used to hold the inner cryostat positions relative to the iron yoke.

The radial stops are shown in Fig. 10. Our original design called for coupling the cryostat to the iron yoke with fixed radial stops between the coil and cryostat at eight azimuthal positions, for both the inner and outer coils. When we analyzed the effect of changes in room temperature on the inner cryostat mounting points and on the outer cryostat push rods, we found that eight fixed positions could generate unacceptable forces. We decided to hold the cryostat at four azimuthal locations, for inner and outer coils. Radial stops at the four fixed cryostat positions were then used for each coil, instead of eight positions. As discussed in a separate section, the decision to support the outer coil radially at only four locations resulted in the outer coil taking an oval shape at just above half field. Three-dimensional modeling then showed the effect, and also that eight stops would be sufficient. We now use eight stops and associated pushrods for the outer coil, and eight radial stops for the inner coils with the inner cryostat boxes locked at four azimuthal locations. Four of the eight push rod sets and all eight of the radial stops of the outer coil are designed with a spring system which becomes active for large forces. The spring-loaded push rods protect against large changes in room temperature. The spring-loaded radial stops preclude very high forces during the cold unpowered condition, but create a "fixed stop" for normal powered conditions.

The heat shields were built from 1.6 mm aluminum sheet, welded to 9.5 mm i.d. aluminum cooling tubes with corner fins (Figs. 8 and 9). The shields are continuous azimuthally, and are hung from the coils with 6.4 mm honeycomb spacers at intervals. G-10 insulated screws with radial slots in the heat shield hold the shield loosely to the coil. The design of concentric rings, heat shield with coil inside, has forced cooldown and warmup to be controlled so that the temperature difference between the shield and coil does not lead to mechanical interference.

Superinsulation blankets were made using 6 μm aluminized Mylar and 0.1 mm polyester spacers with 24 layers/cm. 15 layers were used between the coil and heat shield and 30 layers between the shield and cryostat walls.

At this point the wrapped coil/heat shield was lowered into the U-shaped cryostat box and the straps were attached to the cryostat with clevis and pin. The strap attachment included a vertical screw height adjustment. The accesses for the adjusting screws were sealed with O-ring plugs.

The lead region was treated separately. The outer coil cross-over, carrying current between lower and upper coil blocks, was TIG-welded along the inner edge of the two overlapping leads for 1 m, in steps
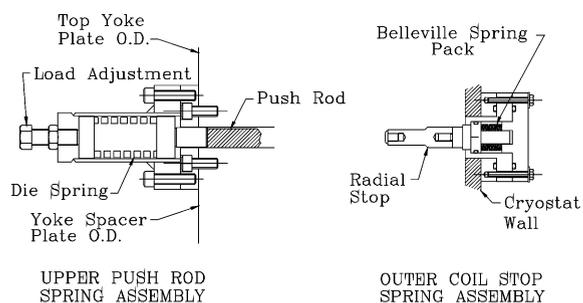

Fig. 10. The spring-loaded radial stop and push rod. The stops are attached to the cryostat inner wall. The push rods preload the outer cryostat, attaching to the yoke at the outer radius, passing through a radial slot in the yoke to the outer cryostat.

of 8 cm in 10 s. In addition, a helium cooling tube was TIG-welded on the inner edge to the conductor over this distance. Only 20–30 cm at each end is uncooled. The leads to and from the outer coil were taken from above and below the upper and inner coil blocks respectively, and were brought together on the midplane separated by 240 μm kapton and the insulation wrapped around the leads (230 μm). The pair was then passed radially through an access hole in the mandrel to the outside radius. The radial sections of the leads are also cooled over their length, with 30 cm uncooled at the coil blocks, and form a radial pair in the transfer line. Cooling tubes were welded above and below the pair in the transfer line. The heat shield was enlarged to the inner radius in this region, as was the cryostat box to accomodate the lead support assembly. Conductor heating from the welding operations was modeled, giving a maximum temperature of 350°C. Degradation of niobium–titanium critical current of 5% was measured for 2 T magnetic field for an annealing time of 10 s for 400°C [8]. A test overlap joint showed a resistance of 16×10^{-9} Ω at 2 T field.

The outer coil was cooled down, before completing the magnet, to test the cooling scheme. This was successful, but a port with O-ring for the inner wall of the outer cryostat was added for access to this critical area. Additionally the heat shield was improved at this time and temperature sensors were included in the uncooled lead region where the conductors are routed radially out of the coil. The flow arrangement for the liquid nitrogen in the heat shield was modified to be parallel for the two tubes, with the flow making one complete turn in azimuth, to improve cooldown time. The flow for helium for the outer mandrel is around the azimuth in one direction, crossing to the second tube, then returning in the other direction. The mandrel is thermally continuous around the azimuth, so that the warm location during cooldown is 180° from the lead region. The heat shield was thermally and electrically separated by a G-10 piece at the lead area, primarily to reduce eddy currents in the heat shield. For the inner coils, the heat shields are electrically and thermally continuous around the azimuth, and both the nitrogen and helium lines make one azimuthal loop.

3.1.3. Cryogenic transfer lines

The transfer lines were built to allow for the radial changes from cooldown, using a large bend radius for the inner coil conductors which are brought radially above and below the magnet to junction boxes on the magnet outer radius, and using a large hairpin loop for the outer coil conductors. Helium cooling tubes were welded to the conductors over the entire length of the transfer lines, and liquid nitrogen heat shields were used over the length. The helium cooling tubes were electrically isolated in the transfer lines.

3.2. Yoke and pole construction

3.2.1. Yoke

The magnet is constructed with 12 30° sectors, to limit the size and weight of the individual parts for ease of fabrication and assembly. Each sector, Fig. 2, is built up of steel plate and consists of an upper and lower yoke separated by a spacer plate. The sector weight is about 57,000 kg, including end supports and additional parts, and the complete magnet weighs approximately 680 metric tons.

It is difficult to find suppliers of quality steel who can roll plate steel to the thickness required for the upper and lower yoke plates. To allow the maximum number of steel suppliers to bid, and to reduce the chances of voids through reduction in thickness during the hot-rolling process, these components have been supplied as two separate plates. The plates were welded together at the interface during the machining step. The spacer plate is also made in two pieces to facilitate installation of beam pipes, transfer lines and electrical connections to the outer coil cryostat.

The upper and lower yoke plates and spacer plates are held in place by eight high-strength steel bolts per sector, extending through all of the plates vertically. These bolts are 5 cm in diameter and were tensioned to 80,000 kg each, which is 57% of the yield point. In addition, the three assemblies, the upper yoke plate, spacer plate and lower yoke plate are doweled together to allow ease of disassembly and reassembly while maintaining their horizontal relationship.

A feature of the overall magnetic design is to have the yoke continuous azimuthally. To achieve

this, each sector end has four radial projections for bolts to fasten adjacent sector ends to each other. When the sectors are fitted to each other, shimmed, and the bolts tightened, relative motion of adjacent sectors is minimized.

Rolled steel plates are specified for the major pieces of steel used in the yoke plates and spacer plates. These have 0.08% carbon maximum with a minimum of alloying elements and impurities. All rolled plates have been completely inspected ultrasonically for voids and the composition of each plate has been determined by chemical analysis. The background information of each piece was retained by a numbering system stamped into the steel pieces.

The lower horizontal face of the upper yoke plate and the upper horizontal face of the lower yoke plate were milled flat within 130 μm and 1.6 μm finish. The inner radius of each yoke plate machining tolerance was to within ± 130 μm of the basic dimension.

Upper and lower surfaces of the spacer plate were milled flat within ± 130 μm and parallel within 180 μm, and thickness accurate to ± 130 μm. Both inner and outer radii of the spacer plate tolerances were within ± 130 μm of the true radius. The as-built vertical yoke gap has an rms deviation of ± 90 μm, or 500 ppm of the total air gap of 20 cm, and a full-width spread of ± 200 μm.

Aximuthal machining requirements were that the sector ends be perpendicular to the gap faces to within ± 0.3 mrad and that the ends be radial to within ± 0.2 mrad. The chords between the outer radius corners of the as-machined sectors have an rms deviation of ± 0.25 mm and a mean of − 0.03 mm. The design azimuthal gap between sectors was 0.5 mm. The as-built azimuthal gaps for the lower yoke average 0.8 mm, with an rms deviation of ± 0.2 mm. Spacer plates and upper sectors were matched to the lower sectors to equalize the effective azimuthal gap for the three pieces, weighted by the magnetic reluctance for each sector.

3.2.2. Poles and wedges

The pole pieces are shown in Fig. 2. The poles directly affect the field quality, while the effect of yoke imperfections is minimized by the air gaps between the yoke and poles. The poles require high-quality steel, with tight machining tolerances on the flatness of the faces which define the storage ring gap. The pole steel was continuous vacuum-cast with 0.004% carbon. The tolerance on flatness was 25 μm, which represents 140 ppm of the storage gap. The surface was ground to a 0.8 μm finish (4 ppm). The pole widths were machined to 56 ± 0.005 cm, and the thickness to 13.3 ± 0.004 cm. The upper and lower faces were machined parallel to 0.005 cm.

In order to control and adjust the pole location and tilt, the poles were constructed in 10° azimuthal sections, compared to the 30° sectors of the yoke. The pole edges that align with the yoke sectors were machined radial, and the middle pole of each sector is interlocking, with a 7° angle from radial. The poles were located azimuthally with 80 μm kapton shims, with the pole edge each 60° in azimuth machined to the correct azimuth. Then kapton was used to electrically isolate the poles from each other to control eddy current effects from field changes, from ramping or quench.

The pole edge-shims were built oversized (4.4 mm thick for the shims on the i.d.; 3.2 mm thick for the o.d. shims) to allow for perturbation adjustment during the magnetic field shimming. The shim width is 5.0 cm. The edge shims are attached to the poles using flathead iron screws, countersunk into the shims every 12 cm in azimuth. This spacing adequately holds the shims from the unstable magnetic force which attempts to short the gap.

The poles are attached to the yoke plates by steel bolts whose heads are counter-bored deeply into the poles (see Fig. 2). The bolts are located in the tapered region of the poles away from the storage region, and the bolt heads are covered by cylindrical plugs of pole steel.

The as-built storage ring gap with a design value of 18 cm was measured using capacitance devices to ± 1 μm accuracy. The gap height varied by ± 23 μm rms with a full range of 130 μm. The tilts of the poles in the radial direction were measured with a precise bubble level and adjusted to ± 50 μrad. The poles were aligned to be horizontal when powered. This required an initial opening angle of 80 μrad toward the ring center to compensate for the asymmetric closing of the gap, as shown in Fig. 11. Adjacent poles were matched to
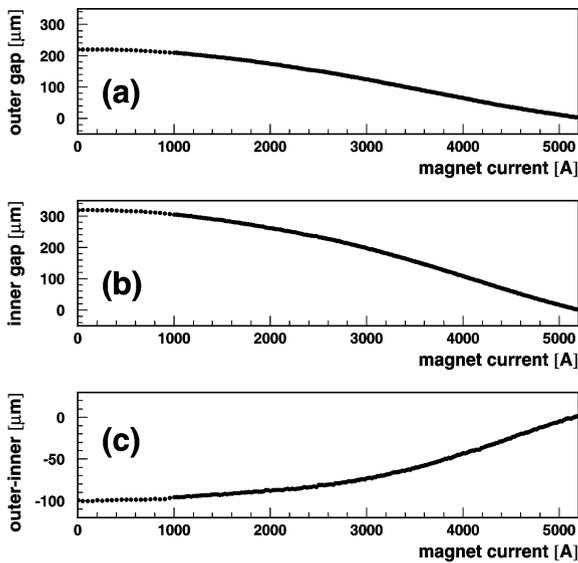
Fig. 11. The measurement of the storage ring gap as a function of magnet current, using the capacitance device described in the text. The gap was measured at $r = +15$ cm (a), and $r = -15$ cm (b), relative to the center of the storage region. The gap values at full field, 5200 A, have been subtracted. The total gap closure as well as the difference (a)–(b) = (c) is in good agreement with stress calculations.

± 10 μm to keep field distortions caused by steps in the iron surface small.

The shimming gaps between the yoke and poles serve three purposes: the gaps decouple the yoke steel from the poles; flat dipole correction coils for each pole are installed in the gaps to adjust the dipole field in azimuth; and the gaps contain iron wedges used to shim the magnetic field. The wedges, sloped radially to provide the C-magnet quadrupole correction, are attached so that they can be adjusted radially. The radial adjustment changes the dipole field locally. The wedges are 9.86 cm wide (azimuthal direction), with 72 per 30° sector. They are 1.65 cm thick on the inner radius, 0.5 cm thick on the outer radius, and are 53 cm long (radial direction). Note that the wedges are rectangular in the r–ϕ plane, so that there is a larger gap azimuthally between the wedges on the outer radius.

A difficulty that we did not anticipate was that the magnetic force direction was quite different at lower field than for full field. The wedge angle is designed to distribute the field lines uniformly radially at full field, with the yoke and wedge iron partly saturated. At lower field, however, the iron is not saturated, and the smaller total gap at the larger radius, where the wedges are thicker, draws more field lines. This leads to a torque on the poles and wedges. To stabilize the wedges, clamps were made from aluminum sheets taped together with the appropriate "anti-wedge" shape. The poles are held in place by the bolts described above, and aluminum/steel laminated spacers are used to hold the poles away from the yokes. At full power the force is 2×10^6 N per pole. The iron lamination in the spacers replaces iron in the wedges that are notched, due to the spacers. There are 24 spacers for each 30° sector, located at the sector ends and at 2.5° azimuthal intervals, on the inner and outer radii of the poles. We measured the torque on a pole during ramp-up (Fig. 12) and confirmed calculations that the pole attachments were sufficient.

3.2.3. Magnet support

The magnet is intended to move as a single rigid body, as much as possible. The magnet supports are located at the 12 sector joints, and are designed to move the sector pairs together. The ring also sits on low-friction pads, and is held to the floor at only one azimuthal position.
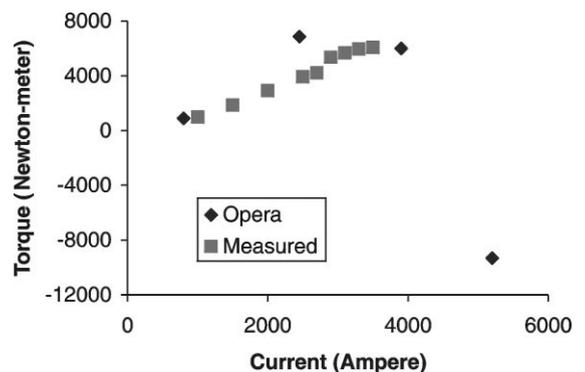

Fig. 12. The measured and calculated torque on a pole during ramp-up, with the pole pivoting about the inner radius spacers. At lower current, the outer radius of the pole tries to short the gap, pulling away from the yoke. The torque at full current, 5200 A, is the opposite sign, with the pole pushing against the spacers toward the yoke.

At the contiguous ends of each sector there is a common base plate of 7.6 cm thick steel. These base plates are solidly bolted and grouted to the floor.

On the top of each baseplate are four 25 ton Duff Norton worm gear screw jacks. These are located to act at the inner and outer radius of the ends of adjacent sectors. The top of each jack has a plate with a low-friction facing to allow the magnet sector to be adjusted radially. The actuating shafts of the jacks at the inner and outer radii are aligned with each other so that after the sectors were positioned the jacks were coupled together. When vertical adjustment is necessary the rotation of one actuating shaft adjusts the vertical sectors together to the proper vertical position without changing their relative positions. Also on the base plate are massive angle brackets with adjusting screws to move the sector ends radially.

To cope with possible horizontal motion of the floor, the four large bolting lugs on the lower and upper yoke assemblies have ground shims placed between the adjacent sectors so that, when the 5 cm bolts in each set of lugs are tensioned, the g-2 magnet yoke acts as a unit and slides on the antifriction pads on top of the jacks. The radial restraint from the brackets on the base plates has been relaxed except for one location. Computer calculations based on the stiffness of the magnet yoke, measured floor motion, and the friction from the sliding pads have shown that the magnet ring is effectively decoupled from the floor motion by this system.

4. Power, protection and cryogenics

4.1. Power supply

Both persistent mode and power supply excitation were considered. The total flux, $\int \boldsymbol{B} \cdot d\boldsymbol{S}$, is conserved in persistent mode. However, room temperature changes would result in changes in the effective area. Thus although the flux is conserved, the magnetic field in the muon storage region is not. Persistent mode would also require a high-current superconducting switch. Power supply excitation with NMR feedback was chosen, although no feedback was used for the 1997 run. This method gives

Table 4
Power supply parameters

Rating	5 V, 6500 A	
Rectifier	480 VAC input, 12 pulse (Two ± 15°, 6 pulse units in parallel)	
Output filter	0.4 F	
Regulator	Low-level system	0.1 ppm stability with 17 bit resolution
	Power section	Series regulator with 504 pass transistors
Cooling	Closed loop water system with temperature regulation	
Regulation	Current–internal DCCT	± 0.3 ppm over minutes to several hours
	Field–NMR feedback (current vernier)	± 0.1 ppm (limited by the electronics noise floor)
Manufacturer	Bruker, Germany	

excellent control of the magnetic field and allows the magnet to be turned off and on easily. The power supply parameters are shown in Table 4.

4.2. Quench protection

The quench protection design parameters were determined by the requirements of magnetic field stability and protection of the magnet system in case of a quench. When the energy is extracted, eddy currents are set up in the iron which oppose the collapse of the field. This can cause a permanent change in the magnetic field distribution [9]. This is sometimes called the "umbrella" effect, since the shape of the change over a pole resembles an umbrella. The eddy currents are minimized if the energy is extracted slowly. There will also be eddy currents in the aluminum mandrels supporting the coils. Electrically, this can be represented by a one

turn shorted transformer. These eddy currents will heat the mandrels and can cause the entire coil to become normal. This is called quench-back. This has several beneficial effects. The part of the stored energy that is deposited in the coil is deposited uniformly over the entire coil and mandrel assembly. Also, once quench-back occurs, the energy extraction process is dominated by the quench-back and not by the specifics of where the quench occurred. Therefore, the effects of a quench on the reproducablility of the magnetic field should be minimal.

The energy extraction system consists of a switch, resistor, and quench detection electronics. An energy extraction resistor of 8 mΩ was chosen. Including the resistor leads, the room temperature resistance is 8.8 mΩ. This gives an L/R time constant of 1 min. The actual time constant varies due to the temperature increase of the coil and dump resistor and the effect of eddy currents in the mandrels during the energy extraction (see below). This resistance value was calculated to cause quench-back in the outer mandrel within 2 s at full current.

The quench protection circuit is shown in Fig. 13. The energy extraction trigger for a quench which originates in one of the coils is the voltage difference between matching coils; for example, V(outer-upper) $-$ V(outer-lower). Since the inductance is effectively the same, the voltages should be equal even while charging the magnet, unless a quench develops in one coil. This quench threshold is set at 0.1 V. However, the coil interconnects are thermally coupled together with the helium tubes. It is possible that a quench in an interconnect could propagate to both coils almost simulta-

neously. Therefore, a voltage threshold of 10 mV was chosen for each interconnect. The outer upper to lower interconnect is only 1 m long. This threshold was set to 5 mV. The thresholds were determined by the requirement that the quench be detected within 0.2 s. The gas-cooled leads develop a voltage of typically 15 mV at full current. If the lead voltage exceeds 30 mV, the energy is extracted.

4.3. Cryogenics system

The storage ring magnet is cooled with two-phase helium flowing through tubes attached to the coil mandrels, to the superconducting coil electrical interconnects, and to the inflector coil package. The superconducting coils are cooled by conduction from the mandrels. The inflector [10] is a superconducting magnet which cancels the field seen by the incoming beam. It will be the subject of a future paper. The flow of two-phase helium is provided by the Joule–Thomson (J–T) circuit of a helium refrigeration plant located in a building near the experiment. The 80 K shields around the coils are cooled with pressurized liquid nitrogen delivered from a liquid nitrogen storage tank. The heat leaks at 4.9 and 80 K into the magnet cryogenic system are given in Table 5.

Table 5
Estimates of cryogenic heat leaks

|		4.9 K load (W)	80 K load (W)
Magnet system heat load	Outer coil cryostat	52	72
	Two inner coils	108	77
	Inflector	8	5
	Interconnects	11	46
	Magnet subtotal	179	200
Distribution	Helium piping	19	
	Control dewar	5	
	Interconnects/valves	33	32
	Nitrogen piping		34
	Distribution subtotal	57	66
Lead gas (1.1 g/s)	Equivalent refrigeration	114	
Total refrigeration		351	266
Contingency		70	51
Cryogenic design	Operating point	421	308
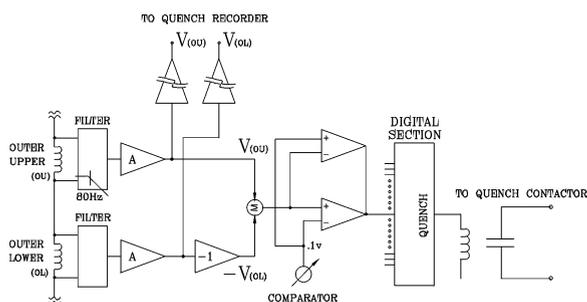
Fig. 13. Diagram of the quench protection circuit.

The helium refrigerator uses a modified Claude cycle with liquid nitrogen precooling. With nitrogen precooling, the refrigerator produces 625 W of cooling at 4.9 K, when it is supplied with 100 g/s of helium at a pressure of 1.8 MPa from a pair of screw compressors. Helium makeup and recovery occurs at the compressor end of the helium system.

The two-phase helium cooling avoids the increase in temperature that would occur in a circuit cooled with single-phase helium. The operating temperature of the coils is within 0.2 K of the coldest temperature in the cooling circuit. The advantages of two-phase cooling are: (1) the helium flows in well-defined flow circuits; (2) the total amount of helium that can be flashed off during a quench is limited to the mass of helium in the magnet cooling tubes; and (3) the location of the helium input and output from the cryostat and the location and orientation of the gas cooled leads are not affected by the cooling system [11].

The key to the operation of a two-phase helium cooling circuit is a helium dewar (the control dewar) that contains a heat exchanger. This heat exchanger sub-cools the helium from the J–T circuit before it enters the magnet cooling circuits. This isobaric cooling provides a higher ratio of liquid to gas with a higher pressure and lower temperature than the refrigerator J–T circuit alone would provide. This feature is important for the long cooling channels in the magnet cooling circuits. The use of a heat exchanger in the control dewar reduces the helium flow circuit pressure drop by a factor of two or more. The control dewar and heat exchanger also have the effect of damping out the oscillations often found in two-phase flow circuits. The helium in the control dewar acts as a buffer providing additional cooling during times when the heat load exceeds the capacity of the refrigerator.

The g-2 cooling system was originally designed to have three separate cooling circuits [12]: a 218 m long cooling circuit that cools all three mandrels in series, the lead and coil interconnect circuits that are 32 m long (the gas-cooled leads are fed off of this circuit), and a 14 m long cooling circuit for the inflector magnet. Later the cooling system was modified to permit each of the mandrels to be cooled separately. Ultimately, the g-2 cooling system operates with parallel cooling circuits for the coils, inflector, and lead cooling. Electrically, the three coils are connected in series so that the two inner coils are in opposition to the outer coil to produce a dipole field between the inner and outer coils. The magnet is powered through a pair of tubular gas-cooled leads developed for this application. Each lead consists of a bundle of five tubes [13,14]. Each tube in the bundle consists of three nested copper tubes with helium flow between the tubes. The copper tubes used in the leads are made from an alloy with a residual resistance ratio of about 64. The lead length is 500 mm. A typical cool down from 300 to 4.9 K takes about 10 d. Once the control dewar starts to accumulate liquid helium, it takes another day to fill the 1000 l dewar.

In operation, the pressure drop [15] across the magnet system is about 0.02 MPa (3.0 psi). We initiated several test quenches and had one unintentional quench when the cooling water was shut off to the compressors. The peak measured pressure during a 5200 A quench was 0.82 MPa (105 psig). Other places in the cooling circuit could have a pressure that is 40% higher. The quench pressure peak occurs 11 s after the start of the quench. The quench pressure pulse is about 12 s long compared to current discharge time constant at 5200 A of 31 s. The outer coil mandrel temperature reaches 38 K after the quench is over. Recooling of the magnet can commence within 5 min of the start of the quench. After a full current quench, it takes about 2 h for the outer coil to become completely superconducting. The inner coils recover more quickly.

5. Magnet operation

5.1. Initial magnet excitation

The magnet was energized to half-field during January, 1996. The magnetic field was extensively mapped. The energy was then extracted with the dump resistor. The field was mapped again. The "umbrella" effect was observed to be about 20 ppm. This is about 10 times less than was observed in the CERN muon storage ring [1] after a power loss. The coil resistance for the CERN magnet was 0.1 Ω. (A smaller effect was observed when the

energy was extracted at full current, as expected due to the saturation of the iron.)

We then attempted to energize the magnet to full current. At 70% of full current, a deep resonant noise was heard originating in the outer cryostat. After 20 s, the energy was extracted by the quench detection system. The quench recording system data were analyzed. The V(outer-upper) $- V$(outer-lower) coil voltage difference exceeded the threshold, which was 50 mV at the time, but the coils did not quench until after the energy was extracted. It seemed plausible that the voltage difference was caused by an upward movement of the outer mandrel and the noise was from scraping on the radial stops. The threshold was increased to 100 mV and the magnet was energized. At 70% of full current an 80 mV voltage difference was observed. When the magnet was ramped down, a 60 mV voltage difference of the opposite sign was observed at 60% of full current. Measurements of the radial magnetic field were subsequently performed. Analysis of the radial magnetic field data (Fig. 14) concluded that the outer coil distorted into a

saddle shape, moving vertically by 4 mm at the maximum, and radially by 2 cm at the maximum. Other measurements were performed which confirmed this picture.

In the following section we present analytic and finite element calculations of the coil stability. These studies were consistent with our observations: at about 70% of full current, a radial instability drove the outer coil into an oval shape. The straps modified the oval shape into a saddle shape. We believe that friction from the mandrel moving across the radial stops caused the noise. A portion of the coil levitated in one area: the straps in that region went from tension to compression. There is about 1 mm free-play in the bushings of the strap attachments. The 1 mm levitation caused the 80 mV voltage difference between the upper and lower outer coils due to $i \mathrm{d}L/\mathrm{d}t$. This is consistent with our flux calculations.

5.2. Coil stability

In this section we begin by discussing our analytic calculations. The outer coil, with its slender cross-section and large diameter, can be distorted by the Lorentz force. It is stabilized by its intrinsic rigidity, the hoop stress induced by the current, and by gravity. The balance of these forces was analyzed to determine the stability limits.

The magnetic force on the outer coil is primarily outwards, 7×10^4 N/m circumference at full field, 1.45 T (5200 A current). But if the coil moves outward the force gets larger, implying a source of instability. The radial gradient of the radial force $\mathrm{d}f_\mathrm{r}/\mathrm{d}r$ has been estimated using OPERA, which gives 38 N/m circumference for a 1 mm distortion. The force is proportional to the current squared.

The strap system supports the coil but does not restrain radial movement. For this reason radial stops are added on the inside, and the mandrel presses against them when cold and powered. In a stable condition, the mandrel presses on these stops equally and slightly deforms symmetrically between each pair of stops, according to the circumference of the mandrel and the radial locations of the stops. A horizontal instability generates an asymmetrical deformation where coil sections between adjacent pairs of stops alternately bow outward

Fig. 14. Measured location of the null in the radial field versus radius R and vertical position Z, for two excitation currents, 1000 A (circles), and 3471 A (squares). The curves show the calculated null in the radial field if the coil were on the midplane (solid line), if the coil were displaced 2 mm upward and 1000 A (dashes), and if the coil were shifted up by 7 mm and 3471 A (dots).

and inward. An example is the case with four stops, where an instability causes the mandrel to take on an oval shape. For n radial stops there can be an unstable perturbation of the radial shape of form $r = A\sin(ks)$, where s is the distance measured along the circumference and $k = n/2\rho$ with $\rho = 7.52$ m, the mean radius of the outer mandrel. This is resisted by the intrinsic rigidity of the beam, determined by its moment of inertia I (1.8×10^{-5} m^4) and Young's modulus E (7.6×10^{10} N/m^2 when the coil is cold).

An additional restoring force comes from the tension $T = F_r \rho$ in the mandrel due to the outward magnetic force F_r. T is proportional to the current squared, and at full current its value is $T_0 = 5.3 \times 10^5$ N. This force is stabilizing as it tends to keep the mandrel circular.

For the assumed distortion of $r = A\sin(ks)$, the total restoring force per unit length on any element of the beam is given by

$$F_{re} = EI\frac{d^4r}{ds^4} - T\frac{d^2r}{ds^2} = (EIk^4 + Tk^2)A\sin(ks). \quad (1)$$

The derestoring force per unit length is

$$F_{de} = \frac{df_r}{dr}r = \frac{df_r}{dr}A\sin(ks). \quad (2)$$

If the ratio $R = F_{de}/F_{re} > 1$ then the system is unstable. R is independent of the assumed value of A and is plotted versus magnet current in Fig. 15, for $n = 4$ and 8 radial stops (The 16 straps supporting the coil are at an angle of 9.9° to the vertical, so a horizontal movement implies also a vertical component. An allowance for this is included in computing the curves in Fig. 15.) The figure shows that four radial stops are insufficient to prevent instability which develops near half of full current, and that eight stops provide stable support for the coil.

At 70% of full current, we observed a severe distortion, but the coil remained stable. The coil was distorting semi-continuously as the current was increased, modified by slip–stick friction against the radial stops. A finite element calculation with a destabilizing force due to an elliptical distortion of 1 cm, and including friction against the
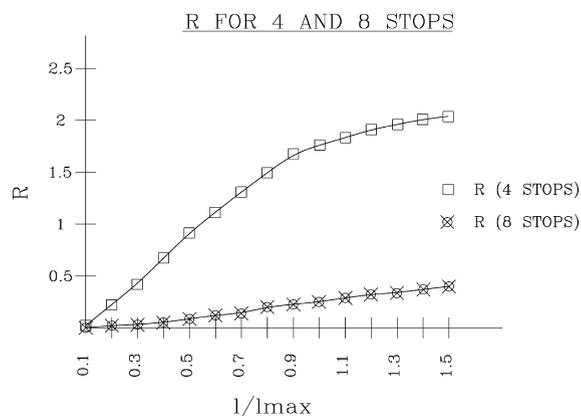

Fig. 15. Analysis showing the ratio of the destabilizing force to the restoring force, versus magnet current, shown for 4 and 8 radial stops.

radial stops, was performed. This gave results consistent with our observations. The analytical calculations indicated the coil would not exceed the stability limit at any current with eight radial stops (see Fig. 15). The finite element calculations also showed much greater stability with eight stops. In retrospect, we failed to realize that a small radial force gradient of 38 N/m circumference for a 1 mm distortion could have such a significant result (the radial force is 7×10^4 N/m circumference).

As discussed in *Cryostat Assembly*, eight fixed coil radial stops and cryostat pushrods would give unacceptable stress. A spring-loaded radial positioner with a limited travel of 2.5 mm was designed to replace the fixed stop (Fig. 10). The mandrel makes contact with the positioner during cooldown at about 85 K. The spring has a pre-load of 3×10^3 N and a spring constant of 4×10^2 N/mm. This spring constant provides a stabilizing force gradient which exceeds the destabilizing gradient of the radial magnetic force. When cold, the spring is compressed by 1.6 mm. The average radius of the mandrel decreases by 2.2 mm as it is cooled from 85 to 5 K, so the coil assumes a slight scalloped shape. At full current, the coil becomes circular. The eight spring-loaded radial positioners with four fixed push rods and four spring-loaded push rods give acceptable stress under all fault conditions studied.

The vertical component of the Lorentz force on the inner upper coil is 1.9×10^4 N/m circumference in the upward direction. There are multifilament straps in 48 locations (two straps in each location) to restrain this force. The horizontal component is only 9×10^2 N/m circumference. Since the inner coils are suspended vertically when cold ($\theta_{strap} = 0°$), the Lorentz force provides a strong restoring force against a radial distortion where $\theta_{strap} = 0° \pm \Delta$. A finite element study of the inner coils was performed. It was concluded that the inner coils were stable against deformation with four radial stops. However, we chose to also use eight radial stops for the inner coils to improve stability and the positioning of the coils.

The new solution with eight radial positioners for each coil was implemented. Strain gauges were placed on the new radial positioners. Also, seven ports with windows were installed in the outer cryostat to view the outer mandrel. In June 1996 the magnet was cooled down and powered to full current. The strain gauge readings and observed coil movement were consistent with the design values. After mapping the field, the energy was extracted. The quench analysis is the subject of the next section of this report.

5.3. Quench tests and analysis

At full field the energy stored in the magnetic field is 6.1×10^6 J. During the magnet commissioning the quench-back mechanism was studied at various currents, ranging from 2% to 100% of the full current. Energy extractions were initiated by opening the dump resistor/power supply switch. During the magnet discharge the coil current and voltages were monitored. In addition, the readings from a set of cryostat temperature probes and pressure gauges were recorded. The cryostat instrumentation was read out every 2 s. The coil voltages and current were recorded every 4 ms during the first 16 s after energy extraction, and every 32 ms for a subsequent 260 s.

5.3.1. Transformer model

If the diode in the circuit is neglected, the magnet and mandrel constitute a transformer which is described by two coupled differential equations

$$L_c \frac{dI_c}{dt} + M \frac{dI_m}{dt} + R_c I_c = V$$

$$L_m \frac{dI_m}{dt} + M \frac{dI_c}{dt} + R_m I_m = 0 \qquad (3)$$

where $I_c = I_c(t)$ and $I_m = I_m(t)$ are coil and mandrel currents. L_c, L_m and $R_c = R_{coil} + R_{leads} + R_{dump}$, R_m denote the inductances and resistances of the coil and mandrel circuits. M is the mutual inductance between the coil and the mandrel. A schematic view of the equivalent circuit is shown in Fig. 16. The external voltage V is 0 when the dump resistor is in the circuit. The solution of the transformer equation (3) is known analytically [16]. For the boundary conditions

$$I_c(t = 0) = I_0, \quad I_c(t = \infty) = 0$$

$$I_m(t = 0) = 0, \quad I_m(t = \infty) = 0 \qquad (4)$$

the coil current is

$$I_c(t) = I_0 \frac{e^{-at}(a^2 - b^2)}{2bR_m} \left[\left(L_m - \frac{R_m}{a+b} \right) e^{-bt} \right.$$

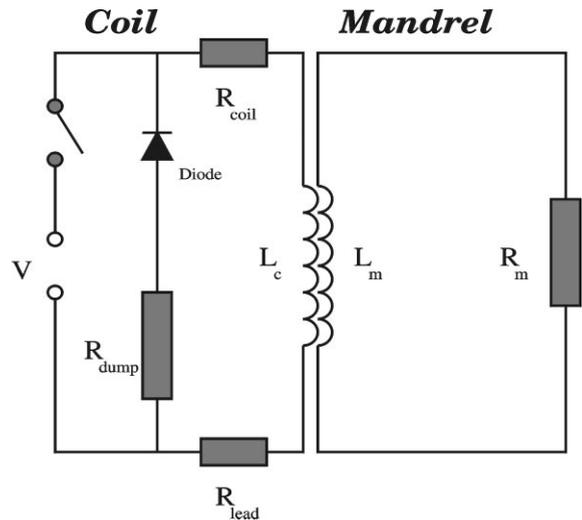$$\left. - \left(L_m - \frac{R_m}{a-b} \right) e^{bt} \right] \qquad (5)$$

Fig. 16. A schematic of the transformer formed by the coil and mandrel of the outer coil. The coil resistance in the text includes the dump resistor, the leads, and the coil.

and the mandrel current is

$$I_m(t) = I_0 \frac{M e^{-at}(a^2 - b^2)}{2bR_m}[e^{-bt} - e^{bt}] \qquad (6)$$

where

$$a = \frac{L_c R_m + L_m R_c}{2(L_c L_m - M^2)}$$

$$b = \left[\frac{(L_c R_m + L_m R_c)^2 - 4R_c R_m(L_c L_m - M^2)}{4(L_c L_m - M^2)^2}\right]^{1/2}. \qquad (7)$$

The energy extraction mechanism was studied during the design stage. For an energy extraction from full current it was predicted that the eddy current heating of the mandrel will cause quench-back after 2 s. The uniform distribution of the energy deposit over the entire mandrel was predicted to result in a modest temperature rise to about 50 K.

5.3.2. Full field quench

Experimentally, quench-back can be detected from the resistive voltage drop $V_R = I_c R$ across the normal conducting zone. The sign of V_R is opposite to the sign of the inductive voltage $L\,dI_c/dt$ associated with the magnet discharge. Fig. 17 displays both inner and outer coil voltages during the initial 6 s of a discharge from full current, $I_c(t=0) = I_0 = 5175$ A. Also shown is the highest outer coil temperature reading (among 8 temperature probes).

In Fig. 17 the coil voltages are shown as a function of time after the energy extraction switch was opened. Quench-back occurred first in the inner lower and the outer lower coils at $t_1 = 1.5$ s. The outer upper coil reaches critical temperature after $t_2 = 2$ s and the inner upper coil at $t_3 = 4$ s. The difference in quench-back time for the two inner coils is attributed to an imbalance in liquid helium flow to the two inner coil cryostats. In contrast, the two outer coil blocks are cooled by the same helium line. However, the cross-section of the outer coil mandrel (Fig. 8) is not symmetric vertically about the horizontal mid-plane due to the mandrel ledges, discounting eddy currents
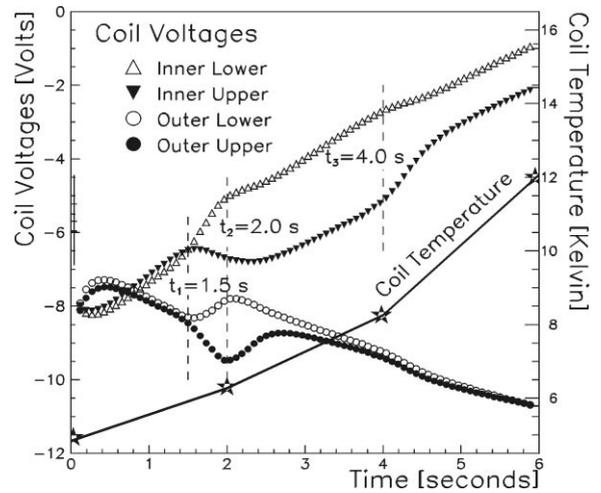

Fig. 17. The measured voltages across the outer coil blocks and the two inner coils are shown for the first 6 s after energy extraction was initiated, from full current of 5175 A. The points shown are averages from data taken every 4 ms. Also shown is the temperature in the outer coil, recorded every 2 s. At $t_1 = 1.5$ s the outer lower coil block and the inner lower coil quench. The maximum temperature at this time is about 5.9 K.

in the coil covers which are not azimuthally continuous. At constant eddy current density this leads to a larger energy deposit in the lower part of the mandrel. Therefore, in agreement with the data in Fig. 17, the outer lower coil is expected to quench first.

The highest observed temperature in the outer coil at quench-back time $t_1 = 1.5$ s was $T = 5.9$ K. This is consistent with the expected critical temperature $T_{critical} = 6.0$ K at full field. At late times, $t \geqslant 100$ s, the maximum outer coil temperature was $T = 37$ K. This temperature was uniform to about 5% in azimuth. Both quench-back time and temperature increase are in reasonable agreement with the design expectations.

Information on the energy deposits into the dump resistor, coil and mandrel is obtained from a fit of $I_c(t)$, Eq. (5), to the recorded magnet current. The fit determines the coil and mandrel inductances, L_c and L_m, as well as their mutual inductance M. Two additional parameters describe the time dependence of the coil resistance which increases from 0 to about 14 mΩ for a discharge from 5175 A. Mandrel and dump resistor lead resistance are
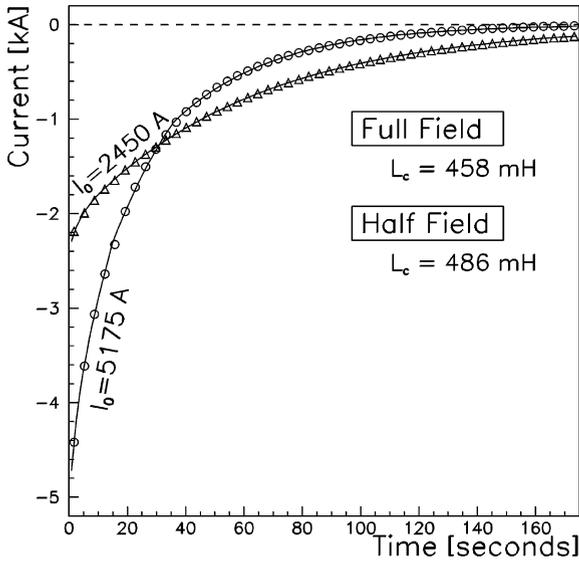
Fig. 18. The coil current $I_c(t)$ from the transformer solution (Eq. (5)) was fitted to measured coil currents. The points shown are averages of data taken at faster sampling rates. The coil inductances and the mutual inductance M were determined from the fit. Shown are data and fit for energy extractions at full field $I_c(t = 0) = 5175$ A and at half field $I_c(t = 0) = 2450$ A. The coil inductances differ by 6% due to the saturation of the yoke iron at high field.

assumed to be constant and are known from earlier analysis: $R_m = 11.6\,\mu\Omega$ and $R_{leads} = 0.9$ mΩ. The dump resistor value is temperature dependent and changes from 8 to 9 mΩ. In the fit an average value of $R_{dump} = 8.5$ mΩ was used. A comparison of the data and fit for magnet discharges from full and half field is shown in Fig. 18. The numerical results from the fit to the 5175 A data are

$$L_c = 458 \pm 5 \text{ mH}, \quad L_m = 0.2 \pm 0.04 \text{ mH},$$

$$M = 8.4 \pm 0.5 \text{ mH}. \tag{8}$$

The outer coil is directly wound onto the mandrel. The coupling between outer coil and mandrel is expected to be close to 1. From earlier measurements and OPERA-2d calculations it is known that $L_{outer\ coil} \approx 0.96 L_c$. The contribution from the inner coils to the flux in the gap is only 4%. Using

$L_c = 458$ mH from fit (8) the predicted values for mandrel and mutual inductance are

$$L_m = \frac{n_m^2}{n_{outer\ coil}^2} L_{outer\ coil} = \frac{0.96}{48^2} L_c = 0.19 \text{ mH}$$

$$M = \sqrt{0.96 L_c L_m} = 9.14 \text{ mH} \tag{9}$$

with $n_m = 1$ for the mandrel and $n_{outer\ coil} = 48$ turns. These values are in good agreement with the results from the fit (8) above and demonstrate the high degree of consistency achieved by modeling coil and mandrel as a transformer.

From the measured coil current $I_c(t)$ and the mandrel current $I_m(t)$ obtained from the fit, Fig. 19, the energies deposited into the dump resistor, mandrel and coil for a full current energy extraction are calculated as

$$E_{dump} = \int_{t=0}^{\infty} (R_{dump} + R_{leads}) I_c^2(t)\,dt = 2.4 \times 10^6 \text{ J}$$

$$E_{mandrel} = \int_{t=0}^{\infty} R_{mandrel} I_m^2(t)\,dt = 1.5 \times 10^6 \text{ J}$$

$$E_{coil} = \tfrac{1}{2} L_c I_c^2(t = 0) - E_{dump}$$

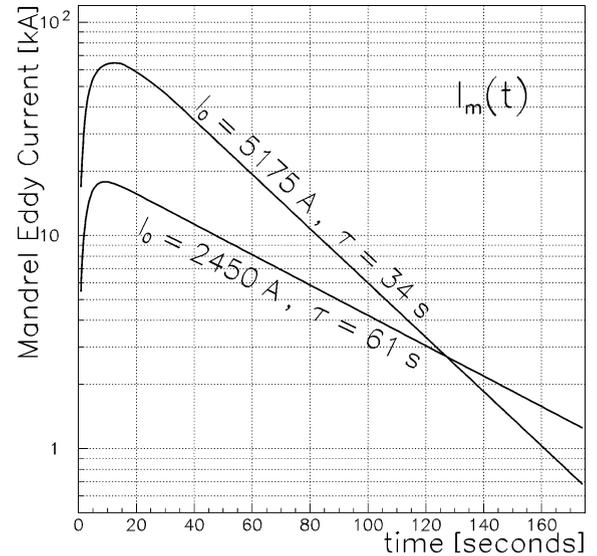$$- E_{mandrel} = 2.2 \times 10^6 \text{ J}. \tag{10}$$

Fig. 19. Eddy currents induced in the outer coil mandrel for magnet discharges from 5175 and 2450 A. The time constants are shown.

The total stored energy is 6.1 MJ. 39% of the stored energy is deposited in the dump resistor, 36% is resistive losses in the coil and 25% in the mandrel. It is estimated that less than 0.08 MJ of the energy deposited in mandrel and coil is absorbed in latent heat of liquid helium. The energy deposit into the diode is 0.11 MJ.

6. Conclusion

The superferric storage ring magnet designed for the precision muon g-2 experiment, with a radius of 7.11 m and a magnetic field of 1.45 T, has been successfully completed and is now operational. The yoke iron was constructed from conventional quality AISI 1006 (0.07% typical carbon content) iron pieces, and the pole pieces from continuous vacuum cast ultra-low-carbon steel (ULCS). The magnet is excited by three superconducting coils connected in series with one coil at the outer radius with a part above the midplane and a part below the midplane, and two coils at the inner radius, above and below the midplane. The conductor in the coil is a niobium–titanium superconductor in a copper matrix with pure aluminum stabilizer. The coils are powered by a low voltage supply providing 5200 A with internal regulation to 0.3 ppm, and NMR feedback capable of 0.1 ppm stability. A two-phase helium cryogenics system cools the coils to 5 K. The quench protection circuit uses as an energy excitation trigger a voltage difference between matching coils.

In order to achieve a highly uniform magnetic field, provision has been made for extensive iron shimming including adjustments to the yoke plates, insertion of iron in the air gaps between the poles and yoke, and adjustment of edge shims on the poles. Surface coils on the poles allow finer control of static and slowly varying errors. Overall homogeniety at the ppm level has been a design criterion.

Initial difficulty in turning on the storage ring to full field, which was associated with strong Lorentz forces and consequent motions of the coil, was overcome by using four additional radial positioners for a total of eight. The storage ring achieved full magnetic field in June, 1996, and shimming began in July. Muons were first stored in 1997 with a first BNL measurement of muon g-2 [17].

The shimming and measurement of the magnetic field over the muon storage region will be reported in a subsequent publication.

References

[1] J. Bailey et al., Nucl. Phys. B 100 (1976) 1.
[2] H. Drumm, C. Eck, G. Petrucci, O. Runolfsson, Nucl. Instr. and Meth. 158 (1979) 347.

[3] G.T. Danby, J.W. Jackson, in: E.R. Lindstron, L.S. Taylor (Eds.), Proceedings of the 1987 IEEE Particle Accelerator Conference, IEEE, New York, 1987, p. 1517.

[4] Reference Manual for the POISSON/SUPERFISH Group of Codes, LANL, LA-UR-87-126.

[5] G.T. Danby, J.W. Jackson, IEEE Trans. Appl. Supercond. 5 (2) (1995) 662.

[6] A. Yamamoto, H. Inoue, H. Hirabayashi, J. Phys. 45 (1984) C1–337.

[7] I. Polk, Development and performance of the glass fiber-epoxy straps, Isabelle Proj. Tech. Note 95, 1979.

[8] Th. Schneider and P. Turowski, Thirteenth International Conference on Magnet Technology, Victoria, Canada, September 1993, Paper R-J-07.

[9] K. Halbach, Nucl. Instr. and Meth. 107 (1973) 529.

[10] F. Krienen, D. Loomba, W. Meng, Nucl. Instr. and Meth. A 283 (1989) 12.

[11] M.A. Green et al., Operation of a two-phase cooling system on a large superconducting magnet, Proceeding of the Eighth International Cryogenic Engineering Conference, Genoa, Italy, June 1980, IPC Science and Technology Press, 1980, p. 72.

[12] L.X. Jia et al., Cryogenics for the muon g-2 superconducting magnet system, Proceedings of the 15th International Cryogenic Engineering Conference, Genoa, Italy, June 7–10, 1994 (Supplement to Cryogenics 34), Butterworth-Heinemann, 1994.

[13] L.X. Jia et al., Design parameters for gas-cooled electrical leads of the g-2 magnets, Proceedings of the 15th International Cryogenic Engineering Conference, Genoa, Italy, June 7–10, 1994 (Supplement to Cryogenics 34), Butterworth-Heinemann, 1994.

[14] M.A. Green et al., in: A Design Method for Multiple Tube Gas-Cooled Electrical Leads for the g-2 Superconducting Magnets, Advances in Cryogenic Engineering, Vol. 42, Plenum Press, New York, 1995.

[15] L.X. Jia et al., in: Cryogenic Tests of the g-2 Superconducting Solenoid Magnet System, Advances in Cryogenic Engineering, Vol. 42, Plenum Press, New York, 1995.

[16] W.M. Schwarz, Intermediate Electromagnetic Theory, Robert E. Krieger Publishing Company, 1973.

[17] R.M. Carey et al., Phys. Rev. Lett. 82 (1999) 1632.